Bulgarian Chemical Communications, Volume 58, Issue 1 (pp. 109-119) 2026 DOI: 10.34049/bcc.58.1.AESMT25-29

Investigation of capillary-porous coatings made of mineral media

A. A. Genbach[1], D. Yu. Bondartsev[1], A. G. Georgiev[2]

[1]*Almaty University of Power Engineering and Telecommunications named after G. Daukeyev, 050013, 126 Baitursynov Str. Almaty, Republic of Kazakhstan*

[2]*University of Telecommunications and Posts, Department of General Engineering, 1 Acad. Stefan Mladenov Str., 1700 Sofia, Bulgaria*

Received: December 16, 2025; Revised: February 01, 2026

Thermal loads for cooling systems with natural material coatings were investigated. The conditions of material spraying on a heating surface were determined. The research had implications for the thermal protection of the equipment. Two most intensive processes were simultaneously used in the cooling methd: (i) interaction of turbulent jet with a barrier and (ii) boiling of the coolant on the heating surface. Devices for spraying of coatings by detonation high-temperature flares were developed. A method of holographic interferometry and high-speed filming was used in the research. Heat fluxes, temperatures, flow rates, and pressures of liquid and gas streams were measured in the experiments. The fabrication of coatings from natural materials can divert higher critical loads and stabilize the surface control process. The characteristics of torches for the generation of supersonic high-temperature detonation flares during the spraying of coatings from powders of natural materials were selected. Due to supersonic flow velocity, spraying occurs without melting of powder particles. The oxidizer excess coefficient varied in the range of 0.3÷0.8; the jet plume temperature (3500÷850) ^{0}C; the jet length (0÷0.16) m; the jet radius (3÷10)×10^{-3} m. The proposed heat exchange mechanism is effective for the process of spraying particles (powders) of mineral media on a heat exchange surface.

Keywords: heat transfer, coatings, mineral media, combustion chamber, nozzle, heat protection.

INTRODUCTION

Natural materials such as tuffs [1, 2], marbles [3, 4], quartzites [5, 6], granites [7, 8], teschenites [9] and bentonites [10] have great potential for high-temperature and high-intensity applications, especially in fields such as thermal power generation [11], cooling systems [12-15] and thermal protection [16]. These materials have long been studied and applied in various fields of renewable energy, construction, engineering, mechanical engineering, and materials science, but their use as coatings for thermal power equipment is a relatively new and promising area [17].

Modern powder materials are not only able to significantly improve the thermal resistance and efficiency of systems, but also provide a high degree of protection against thermal damage, which in turn contributes to increasing the reliability and extending the service life of equipment [18]. The development of new technologies and methods of processing natural materials opens new horizons for their application in a wide variety of industries.

It is highly relevant to conduct scientific studies of heat transfer in capillary-porous natural materials. As such materials rocks such as tuffs, marbles, quartzites, granites and teschenites were chosen. Powders were made from them and sprayed onto the substrate. Based on the physical model in a real capillary porous structure, the heat conduction equations of the thermoelastic problem were written. The solution was obtained for the limiting values of the heat fluxes of melting $q_{\text{mel.}}$, compression $q_{\text{com.}}$ and stretching $q_{\text{ten.}}$, causing the corresponding thermal stresses σ [1, 6]. The model was verified by experiment using high-speed filming of the formed particles (husks) with SKS-1M.

Previously, a scientific research methodology [4] was constructed with an integral experiment [17] to test nine combustion chambers of a thermal tool [6] designed for processing natural mineral media. High-speed filming was used to elucidate the nature of fracture. Along with the study of natural capillary-porous coatings for their limiting state $q_{\text{lim.}}$, $\sigma_{\text{ten.}}$ [1, 9], studies of the boiling heat transfer crisis in capillary-porous structures of metallurgical meshes were conducted [4, 17].

A physical model of the boiling flow was constructed taking into account the joint action of capillary $\Delta P_{\text{cap.}}$ and mass $\Delta P_{\text{cap.+g}}$ forces with excess $m_{\text{l.}}/m_{\text{s.}}$. The mechanism of the heat transfer process was studied by means of holographic interferometry and high-speed motion pictures. Critical specific heat fluxes $q_{\text{cr.}}$ for different pressures P were determined through integral and

*To whom all correspondence should be sent:
E-mail: *d.bondartsev@aues.kz*

thermohydraulic characterizations.

To control the energy processes, the authors of [9] propose to divide the total energy into two components: the energy of the heat wave, the explosively generated vapor nucleus, and the energy of the compressed vapor flow, which is also important for modeling and comparing to boiling processes in the pores of the structure (coating).

The cooling system of various enclosed structures [11], such as combustion chambers [19, 20] and engines [21-24], turbine nozzles [25-28], and tools in the form of rocket burners for coating, has becoming important in thermal power plants. All of the above designs utilize heat transfer.

The authors of [29-31] considered heat transfer in porous coatings in which thermal stresses act. The conditions for the action of thermal stresses σ for the limit state of the surface were developed. The proposed model takes into account the thermomechanical properties of the coating. A complex heat transfer and stress dependence was established for different coating diameters.

However, the authors of [29-31] did not describe the effect of heat transfer and stresses in coatings nor create a calculation methodology.

Today, the task of improving the efficiency of combined energy production [32], as well as cooling the turbine combustion chamber using various coolants to increase the coefficient of performance (CoP) of machines and cycles, remains relevant.

In this paper, the authors present the main scientific and practical results of their research on natural materials, with contributions on:

- natural materials (mineral media in the form of rocks) used for thermal protection of heat-loaded structures;
- creation of a detonation torch of the thermal tool for material spraying on a heating surface.

The scientific novelty of the work includes:

- For the first time, the parameters of the high-temperature supersonic detonation jet of the burner flame were investigated depending on the type of fuel combusted, jet length, inclination angle of the torch tool, and oxidizer excess ratio.
- The phenomenon of spin detonation of the plume at an oxidizer excess ratio less than 1 was registered, and the sputtering process was intensified 2 to 6 times. The range of coating superheating was (20÷75) K. The heat transfer coefficient of the gas jet was about 5-6 times higher than that given by the laminar theory and a few percent lower than that by the law of turbulent heat transfer.

EXPERIMENTAL STUDY OF THE PROCESS OF APPLICATION OF COATINGS BY SPRAYING

For the theoretical study of capillary-porous coatings, the authors of [6] solved a thermoelasticity problem with respect to natural mineral media (natural materials: quartzites, granites, teschenites, marbles, porphyrites, and tuffs). Formulas were derived for calculating the critical specific heat fluxes for melting, compression, and tension, as well as the corresponding thermal stresses acting within the coating [1, 9].

Burners for spraying natural materials have supersonic spin detonation jets. Further development of powder spraying processes is required to create cooling for combustion chambers and increase the efficiency of the elements.

For kerosene-oxygen thermal tools, due to the reduction of water consumption by tens of times, elimination of pumps, simplification of design, and low operating costs, the annual economic effect per one thermal tool is not less than $200-300.

The thermal spraying tool for powder coating deposition is shown in Fig. 1. It enables spraying by means of a pulsating two-phase high-temperature detonation jet. The powder consists of particles of mineral media (quartzite, granite, teschenite, marble, porphyrite, and tuff).

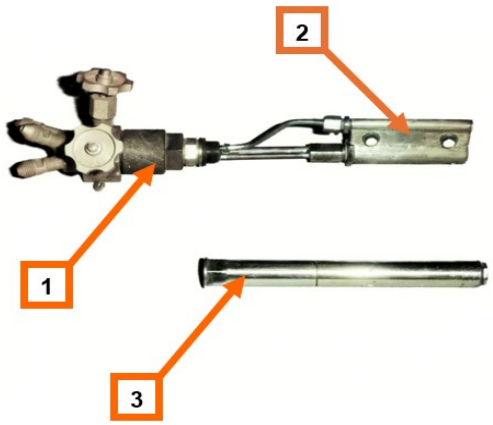

Fig. 1. Installation: 1 - production line, 2 - combustion chamber and nozzle, cooling system for capillary-porous coatings, 3 - casing

Fig. 2 shows an automated production flow line including four detonation torches. Powder spraying was performed on large-sized products, such as shafts with a diameter of 1 m and a length of 4.8 m, metal pipes for heating networks (external coating), balls and sliders.

Fig. 2. Flame pit of the production line with four machine kerosene-oxygen thermal tools, operating in automatic mode, for spraying natural materials on products.

A burner power supply circuit was assembled for conducting an experiment with a thermal tool (see Fig. 3): 1 – collector; 2 – pressure gauge; 3 – collector shut-off valve; 4 – oxygen intake shut-off valve; 5 – ramp reducer; 6 – oxygen cylinder; 7 – air cylinder; 8 – manifold pressure regulator; 9 – three-way valve; 10 – shut-off valve; 11 – water sump; 12 – water hose; 13 – air cylinder; 14 – kerosene cylinder; 15 – shut-off valve; 16 – kerosene sump; 17 – kerosene hose; 18 – plug; 19 – thermal tool; 20 – oxygen hose; 21, 25 – shut-off valves and command reducers; 22, 26 – check valves; 23, 27 – filters; 24 – reactive hose.

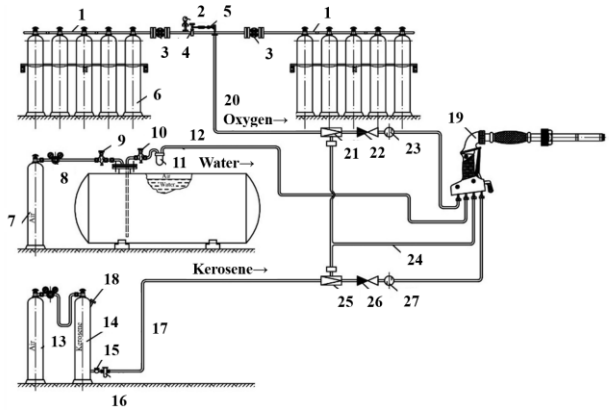

Fig. 3. Displacing power supply circuit of thermal tool.

The heat flows q of the burner jet were measured by a sensor made of a copper cylinder, to which the heat flow of the burner jet was connected from one end, and from the other – the end of the cylinder was cooled by a heat pipe. The side surface of the cylinder was thermally insulated with ceramics based on zirconium dioxide.

Two chromel-alumel thermocouples were placed in the cylinder. The cylinder was attached to a stationary cooled barrier (coating) having an area larger than the jet braking spot area and cooled by a heat pipe. To determine the specific heat flows q on the jet axis and in the braking spot (on the coating) along the radius r, the flow rate G, pressure P and temperature T of the cooler were measured in order to establish the heat balance. Flow rate, fuel and cooler pressure, and in-chamber pressure were also measured.

The holographic interferometry method was used to investigate the coatings. Stresses and strains were studied and recorded in real time. The photographic frequency of the interferograms was 0.5 frames per sec; 30 images were taken from each sample. Photographic prints at two-frame intervals showing the surface condition of the samples every 6 sec were obtained.

Decoding of holographic interferograms was performed according to the accepted methodology. The direction of the displacement vector d was determined.

WAYS TO CONTROL THE PROCESS OF APPLICATION OF COATING BY SPRAYING ON A METAL SUBSTRATE

- *Method of fuel combustion.* Afterburning of fuel (kerosene, gasoline) was performed on a barrier (coating). Oxidizer excess coefficient $\alpha < 1$, burner nozzle - shortened, combustion process - detonation. The afterburning process can be intensified up to two to six times. Oxidizer was added *via* jet to the coating, the fuel in the jet was in excess. Maximum specific fluxes on the barrier: from (2 to 20)×10^6 W/m^2 (Fig. 4). Application mode - without powder melting. Burners served as thermal tools.

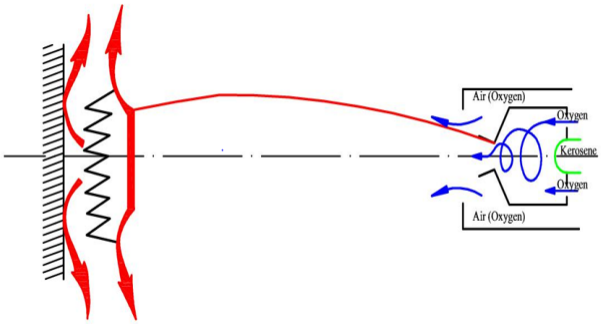

Fig. 4. Detonation after-burning of fuel (kerosene) on the coating surface made of natural material (granite) and a stainless steel substrate.

The afterburning scheme was constructed by observing the process using optical methods (holography, laser GL-38, and high-speed filming SKS-1M).

At gas pressure in the burner combustion chamber of 0.5 MPa (on the coating, the gas pressure is approximately the same), the frequency of pressure fluctuations in the chamber is ≈ (500÷600) Hz, and on the coating (obstacle) is reduced to 200 Hz. This enables the most intensive process of coating spraying and minimizes the possible process of its destruction. Due to supersonic flow velocity, spraying can take place without melting of powder particles.

- *Control of the length of the burner jet flowing out of the nozzle.* The dimensionless jet length is presented in Table 1. For the maximum value of the heat transfer coefficient from the jet to the coating for one of the modes we take α_1 = 1000 W/(m^2×K).

Table 1. Dependence of a/a_1.

a/a_1	0.8	1	0.7	0.4	0.3
z	0	10÷30	40	50	60

For $P_{c.c}$ = 1 MPa, z = (0÷0.16) m, T = (3500÷850) ^{0}C, T_{st} = 3000 ^{0}C – braking temperature (on the coating), t_j = 300 ^{0}C – temperature at the end of the free jet, $r_n = 3\times10^{-3}$ m, $r_j = 10\times10^{-3}$ m (jet radius).

It follows from Table 1 that, along the length of the «barrels» section of the jet, heat exchange decreases, since the boundary layer of the gas is unstable; it partially separates from the heating surface as a result of a sharp pressure fluctuation in the flow behind the wave when the jet meets the coating of this section. The velocity and temperature of the gas decrease along the length z.

- *Adjustment of the jet angle to the coating.* In Table 2, the following is accepted: α_{90} = 1000 W/(m^2×K); T_{st} = 3500 ^{0}C; t_j = 300 ^{0}C; $P_{c.c}$ = 1 MPa.

Table 2. Dependence of a/a_{90}.

a/a_{90}	1	1.1	1	0.8	0.5	0.35	0.3	0.25
β, deg	90	80÷75	60	50	30	20	10	0

As an example, we show in Fig. 5 the texture of a teschenite surface in which a cavern of 2.5×10^{-3} m in size was formed in a time of 2.2 s with q equal to 1.2×10^6 W/m^2 as a consequence of heat transfer deterioration.

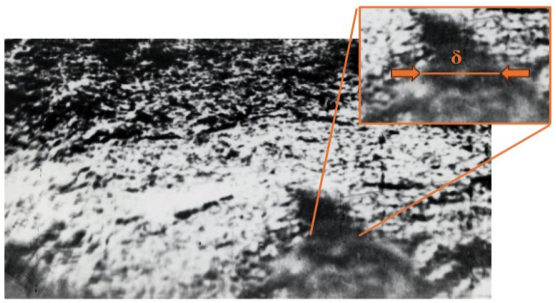

Fig. 5. Texture of the teschenite coating surface with a cavern as a result of thermal degradation ($\delta = 2.5\times10^{-3}$ m).

- *Regulation of the power and type of burners.* For kerosene-oxygen burners of a thermal tool, we have the following characteristics: oxygen consumption G_{oxy} for pressure P_{oxy} = 1.2÷1.5 MPa, m^3/h – 15÷18; kerosene consumption G_{ker} for pressure G_{ker} = 1.3÷1.5 MPa, kg/h – 10÷12; the nozzle critical diameter is d_{nt}, 10^{-3} m – 4÷5; the combustion chamber diameter is d_{cc}, 10^{-3} m – 14.

Gas-dynamic parameters of jets at the outlet of the nozzle are summarized in Table 3.

Table 3. Gas-dynamic parameters of jets at the outlet of the nozzle.

a	$P_{c.c}$ = 1.5 MPa	
	T_g, K	W_g, m/s
0.7	2670	2420
0.8	2780	2410
0.9	2830	2400
1	2810	2320

Fig. 6 shows the technique and technology of thermal tool operation with $d_{nt} = (4\div5)\times10^{-3}$ m, $d_{cc} = 14\times10^{-3}$ m to granite impact surface. The flame structure, jet spreading radius (braking spot), the distance from the nozzle edge (outlet part) of the burner to the coating are visible.

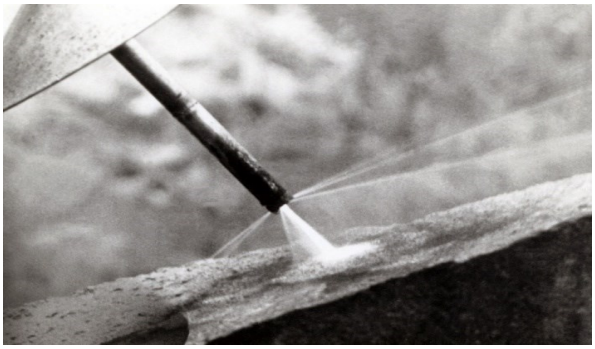

Fig. 6. Position of detonation supersonic flame.

Removal of cooling water from the impact surface in the form of jets was carried out for technological reasons of applying a protective coating (see Fig. 7). The protective shield is designed to protect the worker-operator of the thermal tool.

Specific heat flows q on the coating surface were (5÷12) MW/m^2 for r = 0 and l = (4÷12)×10^{-2} m; (2÷5) MW/m^2 for r = 4×10^{-2} m and l = (4÷12)×10^{-2} m.

Distribution of q (r):

$$q\,(r) = q_{max} \times \exp\,(-1000 \times r^2),\ \mathrm{W/m^2},$$

For a more powerful burner with d_{nt} = 6×10^{-3} m, d_{cc} = 18×10^{-3} m: G_{oxy} for G_{oxy} = 1.8 MPa, m^3/h – 30÷55; G_{ker} for P_{ker} = (1.8-2) MPa, kg/h – 14÷18, we have q (r = 0) = (6÷13) MW/m^2.

Fig.7. Position of the torch to the granite processing surface: 1 - structure of the torch.

The value of heat flows q can be reduced by one order when switching to another type of burner: benzo (kerosene) - air burner. Such burners are used for application of coating by spraying mineral media with a lower strength value than that of quartz or granite, for example, teschenite, porphyrite or marble.

The melting method was used to create coatings from natural and artificial mineral media (volcanic products of eruption, ashes and slags of industrial enterprises in metallurgy and power plants, tuffs). A more powerful thermal tool with a dual burner with d_{nt} = 5×10^{-3} m was used.

The studied thermal characteristics of coatings made of natural materials are related to high-intensity cooling systems. The comparison shows the advantages of boiling in bulk, in thin films and in heat pipes.

RESULTS AND DISCUSSION

Studies on modern surface and coating technologies usually focus on the integrity of thermally sprayed coatings on metals and alloys under the action of tensile stresses and strains [33-35].

However, for the limiting state of natural CPCs formed of mineral media, at certain particle sizes δ and exposure times of the specific heat flux q, compressive stresses play a decisive role in coating failure [1, 9]. Moreover, different thermal spraying methods - atmospheric plasma spraying [36], high-velocity oxy-fuel spraying [37], and high-velocity air-fuel spraying [38] - produce different microstructures and different ratios of compressive, tensile, and shear stresses to strain.

This behavior is associated with the inter-particle bonding strength of the mineral medium, since fully or partially molten powder particles impact and solidify on the substrate, while the degree of bonding between metal particles may amount to only 20÷80% of the particle boundary surface area.

Thermally formed CPCs (see Figs. 2 and 4) are inherently anisotropic, which is advantageous during the cooling process, as capillary forces contribute more actively to the uniform distribution of the cooling fluid.

Assessment of coating stress effects reduces the probability of crack initiation during the development of new devices [4] and enables control over the propagation of critical cracks. A coating with three thermal sources acts as a screen that absorbs shock and detonation waves generated by the thermal tool jet.

Optical investigation methods [17] revealed the damage mechanisms of CPCs at the crack tip, where microstructural features lead to microscopic fracture events. A holographic experimental setup is described in [39]. As an example, interference holograms of CPCs produced from granite (Fig. 8) with a porosity of ε = 5%, as well as from viscous rock with ε = 30% - tuff (see Fig. 9) and marble (see Fig. 10) - are presented. Depending on the properties of the substrate material, the coatings form two media acting as thermodynamic and acoustic screens with three thermal sources, and provide control over the thermal wave penetrating the cooling surface of the combustion chamber and nozzle (see Fig. 1).

CPPs with low porosity (Fig. 8) are in a highly stressed state compared with viscous and porous media (Figs. 9 and 10). A twofold increase in q resulted in up to a threefold increase in surface strain for these coatings, whereas for samples with higher porosity the increase was only about 1.5 times. The number of interference fringes is higher for granite and marble coatings, as they exhibit higher thermal stresses.

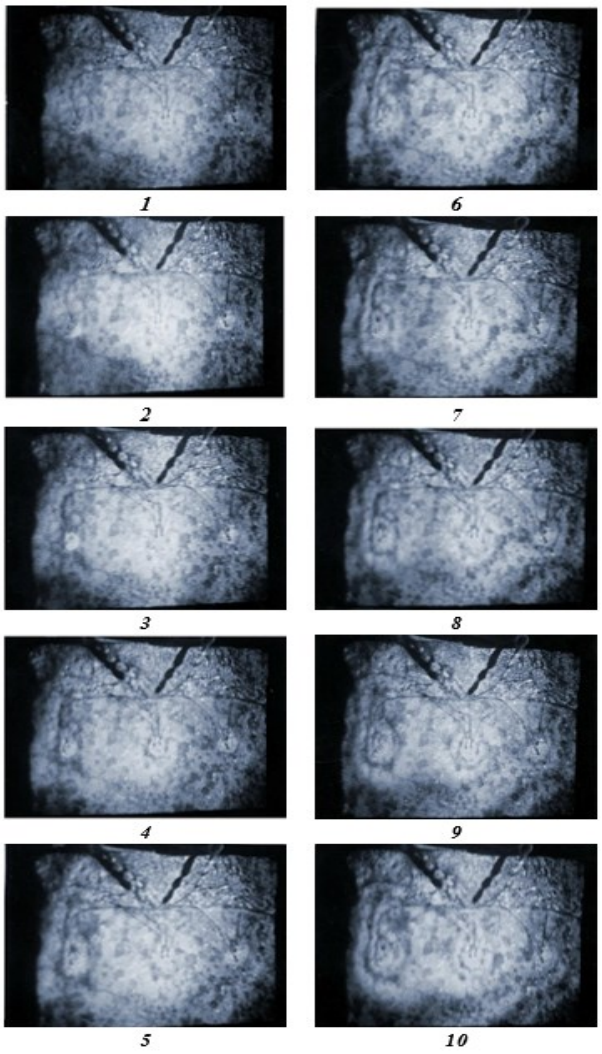

Fig. 8. Holographic interferograms of coatings produced of granite: 1 - τ = 6 s; 2 - τ = 12 s; 3 - τ = 18 s; 4 - τ = 24 s; 5 - τ = 30 s; 6 - τ = 36 s; 7 - τ = 42 s; 8 - τ = 48 s; 9 - τ = 54 s; 10 - τ = 60 s.

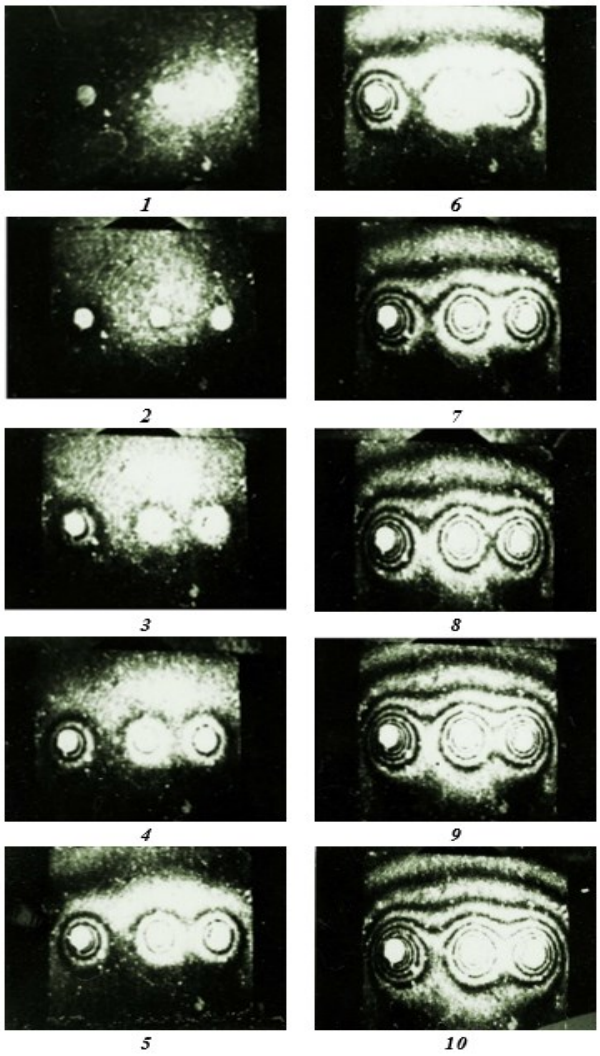

Fig. 9. Holographic interferograms of coatings produced of tuff: 1 - τ = 6 s; 2 - τ = 12 s; 3 - τ = 18 s; 4 - τ = 24 s; 5 - τ = 30 s; 6 - τ = 36 s; 7 - τ = 42 s; 8 - τ = 48 s; 9 - τ = 54 s; 10 - τ = 60 s.

Interferograms made it possible to detect surface defects and cracks in the coatings that were not visually observable, as well as large inclusions in whose regions the equal-strain lines exhibited discontinuities.

For interferometric investigations, the reference point is always the residual strain in the CPC, determined by a network of fine cracks that do not disappear upon removal of the thermal load.

Decoding the interferograms (Figs. 8, 9, 10) for all coatings reveals a nonlinear particle displacement curve [6], with the oxy-kerosene spraying method (see Fig. 4) offering the advantage that particle melting in the CPC is achieved using a spin detonation jet on the coating surface. This significantly reduces powder particle fracture along the boundaries of unmelted particles within the CPC.

For tuff particles, a high degree of particle melting is achieved by increasing the thermal tool power through the use of paired burners. This results in the melting of a large number of random defects formed during CPC fabrication, as well as the elimination of existing voids and caverns. The integrity of the CPC ensures the highest erosion resistance of the coating.

Strain interferograms (Figs. 8, 9, 10) demonstrate that expansion of the coating sample initially occurs around the heat source, and subsequently throughout the volume in which the temperature field is distributed. Failure of the capillary-porous material is expected when microcracks concentrate along the developing fracture zone. After this stage, the crack reaches its critical size, leading to coating failure.

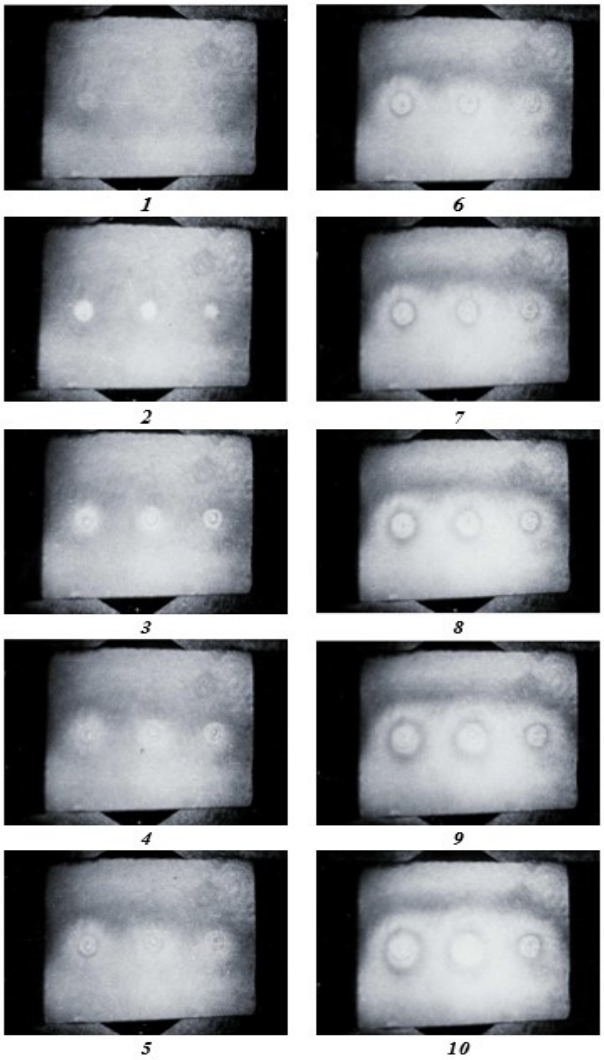

Fig. 10. Holographic interferograms of coatings produced of marble: 1 - τ = 6 s; 2 - τ = 12 s; 3 - τ = 18 s; 4 - τ = 24 s; 5 - τ = 30 s; 6 - τ = 36 s; 7 - τ = 42 s; 8 - τ = 48 s; 9 - τ = 54 s; 10 - τ = 60 s.

To elucidate the mechanism of coating failure, additional methods were employed, including high-speed cinematography using the SKS-1M system [39], the photoelasticity method [6], and analytical solutions of thermoelastic problems [9].

Calculation models [4] use integral values and cannot predict local failures. Optical methods, however, allow the reliability of coating performance to be forecasted. On the interferograms (see Figs. 8, 9, 10), these processes are manifested as line concentrations, including densification, pore collapse, development of tensile microcracks, layer shear, and compression, all oriented in the direction of maximum thermal stress. Optical methods enable the study of coating failure, controlling the loading rate of the specific heat flux q from seconds to hours, providing the required detailed analysis of coating rupture events.

Nonlinear fracture mechanics [1] explains the experimental results, while optical investigation methods [39, 40] reveal the physical mechanisms of material failure (damage) processes. Linear elastic fracture mechanics does not describe the limiting state of CPCs [9], nor the associated stresses, strains, displacements, or damage, since these arise from non-local inelastic energy dissipation processes near the epicenter of failure (the crack tip).

Our application of elliptical particle comminution methods [6] achieves a particle size d smaller than the CPC thickness δ ($d < \delta$). In this case, a size effect becomes apparent, whereby in the notch (groove), damage tends to propagate through the full thickness, making the application of linear-elastic fracture mechanics to CPCs possible. Inelastic processes within the fracture zone will occur at the grain level d.

The inequality $\delta \gtrless d$ results in the CPC being in a transitional zone, in which neither size-independent plasticity theory nor linear-elastic fracture mechanics can provide accurate predictions, and the assumption of a homogeneous CPC does not hold. The CPC is anisotropic, which, however, is advantageous for the cooling system.

Since microcracks in mineral samples initiate from the notch (groove) and model boundaries and subsequently propagate toward the sample center, acoustic and thermodynamic screens have been constructed at the center of the CPC to compensate for crack waves [39].

The energy of the fracture process zone at the sample center where the screens are installed, is primarily expended on the formation of two new free surfaces from the viewpoint of energy dissipation under the maximum specific thermal load q, according to linear-elastic fracture mechanics.

Moreover, plastic processes within the sample and microcracks ahead of the crack tip also dissipate energy, demonstrating the inelastic nature of the crack tip. The combined action of these two mechanisms produces a stress-shielding effect at the crack tip [9].

Studies on the limiting state of CPCs have shown [1] that microstructural features govern the mechanisms of energy dissipation leading to macroscopic failure (q_{max} and σ_{max} in compression, tension, melting, and shear). Additionally, this model presented experimental results using high-speed cinematography.

The phenomenon of crack coalescence, which initiates in the notch (groove) and in other stress concentration regions, such as grain and particle boundaries in CPPs, propagates along the cleavage planes of the CPC, demonstrating the influence of

sample scaling. Although such studies are considered semi-blind, they allow the modelling of sample dimensions, CPC strength, and verification using optical methods [17, 39].

Experimental predictions were offered for local zones (CPP fracture cavities) and in integral form as thermal load–displacement curves, i.e., $q = f(\Delta T)$ and $q = f(\tau, \delta)$ [4, 9].

When applying the theory of the limiting state of the CPC surface (or metallic substrate) based on elastic fracture (thermoelasticity), the importance of investigating local nonlinear failure using optical methods is demonstrated; these methods must be employed during both experimentation and modelling. This is particularly important when the fracture process zone is significant relative to the size of the sample or structure.

In all studies of mineral media, the processes of modelling (or experimental prediction) and analytical calculations are semi-blind and depend on the size (geometry) of the local crack zone in the sample or coating.

For example, the effect of rock thickness (size) on the fracture process induced by the thermal jet is evident (see Fig. 6), where the thickness must exceed a critical value for «spalling» to occur. Otherwise, the processed CPC plate will fail according to scaling laws.

The analogy of the failure process across different materials follows from several considerations. The failure rate υ of the CPC is:

$$\upsilon = \frac{q}{c \cdot \rho \cdot \Delta t}, \text{ m/s}$$

where $\Delta t = t_w - t_f$.

The increase in υ with decreasing Δt is associated with the fact that, during coating heating, the temperature at the surface t_w and at the outer surface of the layer being destroyed t_f become similar due to the intense heat flux q. This promotes volumetric failure of the coating and destruction of a layer of a given thickness.

The surface temperature of quartz and quartz-containing rocks should not exceed 1350 °C, since at temperatures of 1200÷1350 °C, α-quartz rapidly transforms into α-cristobalite without melting, accompanied by a volumetric expansion of +17.4 %.

Another phase transformation occurs at 870 °C, where α-quartz converts to α-tridymite, resulting in volumetric expansion of +12.7 %.

The maximum failure rate occurs at Δt = 100÷200 °C and q > (2÷3)×10^6 W/m², reaching 5÷15 m/h for quartz with ρ = 2500÷2700 kg/m³ and c = (1÷1.2) kJ/(kg×K).

The displacement gradient which determines the magnitude of strain for a single heat source, is greatest in the region of the heater with a radius up to 10×10^{-3} m and increases with prolonged thermal exposure.

Displacement distributions in the plane of the centers of three heat sources (Fig. 11) and in a plane parallel to the centers of the heat sources (Fig. 12) are presented as functions of time for the sample surface under various thermal exposures. The cooling system, implemented as coatings of natural materials, allows for an increase in the critical thermal loads for the thermal tool and the limiting state of the thermal protection coating surface.

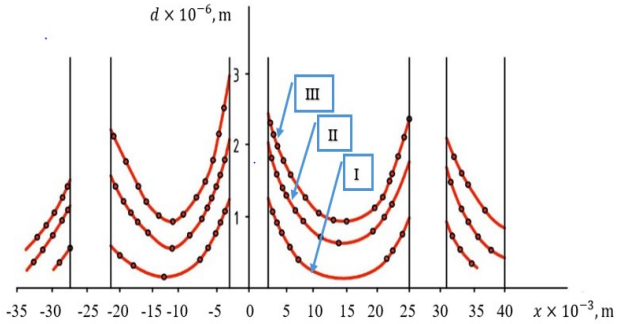

Fig. 11. Dependence of the displacements along the plane of the centers of three heat sources [(y = 0): I – t = 15 s; II – t = 25 s; III – t = 30 s; angle – 38 ^{0} 55′] tuff coating surfaces for different q values

The temperature gradient controls the CPC, thermotechnical properties, thermal stresses, deformations and particle movements in the coating and creates synergistic reinforcement in the graded natural material. The natural coating causes deformation of the substrate at coating temperatures when the thermal stresses are small due to adhesion or curing of the coating. The substrate will absorb dangerous tensile stresses $\sigma_{tens.}$

A different situation can also occur. The stability of mineral coatings is related to the change of tensile and compressive stresses, which we have shown by solving the thermoelastic problem [1]. If it turns out that α of the coating is larger than that of the substrate, the sign of the thermal stress will change. Therefore, it is possible to choose close values of α for the coating and the substrate. For example, quartz perpendicular to the axis base has α = 1.37×10^{-5} K^{-1}, while marble has α = 1.3×10^{-5} K^{-1} (linear expansion coefficient).

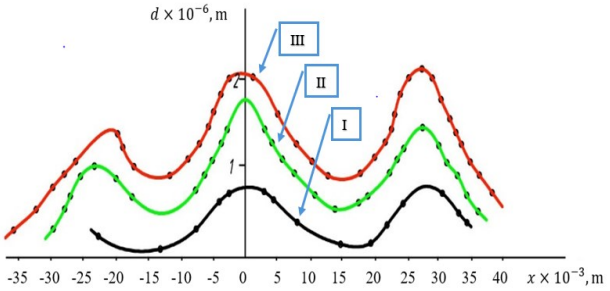

Fig. 12. Dependence of displacements along a plane parallel to the plane of the centers of heat sources [(y = 6×10^{-3} m] of the tuff coating surface for different q values (see Fig. 11),

In the general case we have a rather large choice not only of the value of α, but also of the value of λ. The variation limits for rocks are given in Table 4.

Table 4. Limits of change in natural materials.

λ, W/(m×K)	0.2 ÷ 12
α, K^{-1}	$(0.2 \div 10)\times10^{-5}$

An assessment of the high-intensity cooling system was conducted. The limiting thermal load ranges for CPCs composed of natural mineral media are as follows: teschenite coatings – $(2.1\div4)\times10^6$ W/m², granite coatings – $(4\div6)\times10^6$ W/m², and quartz coatings – $(6.2\div15)\times10^6$ W/m². The thermal loads were within the surface superheating range relative to the saturated steam temperature, $\Delta T = T_w - T_s = (20\div75)$ K.

Under exposure to the rocket torch jet on the CPC (see Fig. 7), the particles of the material undergoing destruction near the heating surface are in a complex stress state (see Figs. 8, 9, 10). They simultaneously experience compressive, tensile, and bending deformations [6].

Compressive stresses σ_{comp} are greatest in the heated layer (Fig. 13). As the distance from the heated CPC increases (l grows), these stresses rapidly decrease, transform into tensile stresses σ_{tens}, reach a maximum at a certain distance, and then diminish. In other words, the criterion $(\alpha\times l)/\lambda$ (the Nusselt number) increases, where α is the heat transfer coefficient, l is the distance from the jet to the CPC, and λ is the thermal conductivity of the coating.

For a CPC material with thermal conductivity λ and heat transfer coefficient α, there exists a minimum layer thickness. If the material thickness is less than L (the calculated thickness of the material undergoing destruction), no σ_f due to spalling develops within the material. The critical thickness l_{cr} is several mm (determined from Figs. 11 and 12).

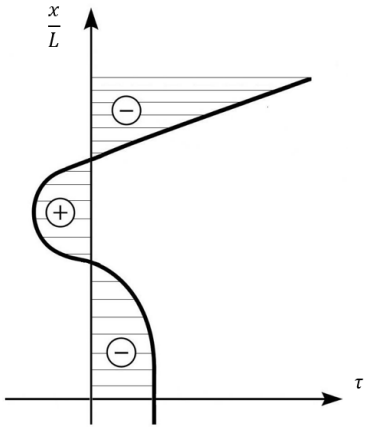

Fig. 13. Diagram of the distribution of compressive and tensile stresses in the heated layer of the CPC

The calculated thickness of the CPC undergoing destruction corresponds to the portion of the rock layer involved in deformation during which destructive stresses develop, which depends on the coating properties and the jet parameters.

At high q [4, 17] and α, stresses σ appear instantly in the heated layer, rapidly reaching maximum values. Then, they quickly decrease, approaching the lower limit (see Fig. 13).

Thus, the greatest compressive stresses arise at the heated surface. These stresses decrease with distance from the surface, transform into tensile stresses, increase to a maximum, and then decrease again, becoming low compressive stresses at greater depths. At high q values (see Fig. 13), CPC failure may occur due to chipping or shear stresses induced by compression. Typically, CPC failure manifests as detachment of particles from the coating surface (see Figs. 8, 9, 10).

The cross-sections where σ_f^{max} occurs are located at 0.2÷0.3 of the calculated thickness from the heated surface, depending on τ and λ.

For $(\alpha\times L)/\lambda = 1$, $\sigma_f/\sigma_{comp} = 0.52$, while for $(\alpha\times L)/\lambda = 20 \rightarrow \sigma_f/\sigma_{comp} = 0.3$. The CPC layer must develop sufficient destructive stresses within a time τ equal to or less than that required to reach the maximum possible stress under the given conditions, i.e., $\tau_f^{comp} \le \tau_f^{comp.max}$; $\tau_f^{ten} \le \tau_f^{ten.max}$.

The values of q and α must be such that stresses in the layer, and consequently its failure, occur before the maximum allowable stresses are reached. With increasing q and α, it is necessary to account for the delayed occurrence of σ_f^{max} relative to the onset of surface heating; otherwise, in viscous CPCs (Fig. 10), premature melting of the material may occur.

CONCLUSIONS

1. Efficient and controllable spraying of coatings made of various natural materials was achieved due to the dynamic characteristics of the detonation torch of thermal tools. The main parameters of coatings were identified and ways to control the spraying processes were investigated.

2. Dependencies for porous coatings under thermal loads are useful for predicting the performance of equipment (nozzles and combustion chambers), and the strain concentration in the coating was studied at thermal loads up to 4.2×10^6 W/m^2.

3. The cooling system showed high efficiency up to the critical state of the metal of combustion chambers and nozzles (5×10^6 W/m^2).

4. The developed surfaces in the form of coatings and mesh structures provide positive effects due to the advantage of joint technologies for their fabrication with the expansion of the dissipated thermal loads and control of the coating condition.

NOMENCLATURE

l – distance from the nozzle section to the coating, m;
z – jet abscissa, m;
α – oxidizer excess factor, heat transfer factor, W/(m^2×K);
ε – porosity;
σ – thermomechanical stresses, Pa;
q – specific heat flux, W/m^2;
q_{cr} – critical (limit) heat flow, W/m^2;
δ – coating thickness, particle size, m;
τ_i – time, s;
P – pressure, Pa;
R_{ox}, R_{ker} – pressure of oxygen, kerosene, Pa;
$P_{c.c.}$ – pressure in the combustion chamber, Pa;
r – radius of the braking spot, m;
n – efficiency factor of a heat power plant.

REFERENCES

1. A. A. Genbach, D. Yu. Bondartsev, I. K. Iliev, *Bulgarian Chemical Communications*, **50**, 133 (2018).
2. Z. Ting, L. Xianglong, W. Jianguo, H. Qiwen, T. Zihao, H. Tao, *Engineering Failure Analysis*, **163**, 108584 (2024) https://doi.org/10.1016/j.engfailanal.2024.108584
3. Z. Yan, M. Chunchi, G. Yaohui, M. Kai, *Transportation Geotechnics*, **47**, 101270 (2024) https://doi.org/10.1016/j.trgeo.2024.101270
4. A. Genbach, H. Beloev, D. Bondartsev, *Energies*, **14**, 6365 (2021) https://doi.org/10.3390/en14196365
5. W. Chen, W. Liu, Y. Liang, *Fluid Dynamics and Materials Processing*, **20**(4), 859 (2024) https://doi.org/10.32604/fdmp.2023.029310
6. A. A. Genbach, D. Y. Bondartsev, *Russian Engineering Research*, **40**, 384 (2020) https://doi.org/10.3103/S1068798X20050093
7. C. Ramadji, A. Messan, E. Prud'Homme, *Materials*, **13**, 5406 (2020) https://doi.org/10.3390/ma13235406
8. W. Ju, D. Feng, L. Yi, T. Hao, Z. Pan, *Journal of Rock Mechanics and Geotechnical Engineering*, volume, page (2024) https://doi.org/10.1016/j.jrmge.2024.09.007
9. A. Genbach, D. Bondartsev, I. Iliev, A. Terziev, *E3S Web of Conferences*, **85**, 05003 (2019) https://doi.org/10.1051/e3sconf/20198505003
10. A. A. Askalany, S. J. Ernst, P. C. Hügenell, H. J. Bart, S. K. Henninger, A. S. Alsaman, *Energy*, **141**, 782e91 (2017) https://doi.org/10.1016/j.energy.2017.07.171
11. National Research Council. Coatings for high-temperature structural materials: trends and opportunities. Washington, DC: The National Academies Press (1996) https://doi.org/10.17226/5038
12. O. S. Sanjay, B. N. Prasad, *Applied Thermal Engineering*, **28** (17-18), 2315 (2008) https://doi.org/10.1016/j.applthermaleng.2008.01.022
13. M. Heyang, W. Zhongwei, N. Yaobin, *Applied Thermal Engineering*, **179**, 115751 (2020) https://doi.org/10.1016/j.applthermaleng.2020.115751
14. S.S. Baakeem, J. Orfi, H. Al-Ansary, *Applied Thermal Engineering*, **138**, 417 (2018) https://doi.org/10.1016/j.applthermaleng.2018.04.018
15. W. Wróblewski, *Applied Thermal Engineering*, **51** (1-2), 953 (2013) https://doi.org/10.1016/j.applthermaleng.2012.10.048
16. G. Jian-Jun, C. Yue, Y. Zheng-Wei, C. Bing, G. Chun-Lin, *Applied Thermal Engineering*, **159**, 113938 (2019) https://doi.org/10.1016/j.applthermaleng.2019.113938
17. A. A. Genbatch, D. Y. Bondartsev, *News of the National Academy of Sciences of the Republic of Kazakhstan-Series of Geology and Technical Sciences*, **2**, 81 (2018).
18. P. Vögelin, G. Georges, K. Boulouchos, *Energy*, **125**, 356 (2017) https://doi.org/10.1016/j.energy.2017.02.113
19. P. Zlateva, N. Penkova, K. Krumov, Analysis of combustion efficiency at boilers operating on different fuels, *Proceedings 7th International Conference on Energy Efficiency and Agricultural Engineering*, 9278784 (2020) https://doi.org/10.1109/EEAE49144.2020.9278784
20. Q. Fu, W. Song, G. Jiao, *Energy*, **266**, 126438 (2023) https://doi.org/10.1016/j.energy.2022.126438
21. Z. Wang, Y. Feng, F. Chen, J. Qin, *Energy*, **314**, 134166 (2025) https://doi.org/10.1016/j.energy.2024.134166
22. K. M. Kim, Y. H. Jeon, N. Yun, D. H. Lee, H. H. Cho, *Energy*, **36**(2), 942 (2011) https://doi.org/10.1016/j.energy.2010.12.016
23. K. Yordanov, T. Mechkarova, A. Stoyanova, P. Zlateva, in: A. Abraham, S. Kovalev, V. Tarassov,

V. Snasel, M. Vasileva, A. Sukhanov (eds.) Proceedings of the Second International Scientific Conference «Intelligent Information Technologies for Industry» (IITI'17). IITI 2017. Advances in Intelligent Systems and Computing, 680 (2018) https://doi.org/10.1007/978-3-319-68324-9-44
24. J. Xu, K. Cheng, C. Dang, Y. Wang, Z. Liu, J. Qin, X. Liu, *Energy*, **275**, 127488 (2023) https://doi.org/10.1016/j.energy.2023.127488
25. W. Wang, J. Gao, X. Shi, L. Xu, Cooling performance analysis of steam cooled gas turbine nozzle guide vane, *Int. J. of Heat & Mass Transfer*, **62**, 668 (2013), https:// doi.org/10.1016/j.ijheatmasstransfer.2013.02.080
26. S. W. Moon, H. M. Kwon, T. S. Kim, D. W. Kang, J. L. Sohn, *Energy*, **160**, 625 (2018) https://doi.org/10.1016/j.energy.2018.07.035
27. X. Yang, Z. Liu, Z. Feng, T. Simon, *Int. J. of Heat & Mass Transfer*, **140**, 25 (2019) https://doi.org/10.1016/j.ijheatmasstransfer.2019.05.109
28. W. Wang, *Int. J. of Heat & Mass Transfer*, **80**, 217 (2015) https://doi.org/10.1016/j.ijheatmasstransfer.2014.09.024
29. R. Boubaker, V. Platel, *Energy*, **111**, 402 (2016) https://doi.org/10.1016/j.energy.2016.05.102
30. G. Lei, W. Li, Q. Wen, *International Journal of Thermal Sciences*, **137**, 55 (2019) https://doi.org/10.1016/j.ijthermalsci.2018.11.017
31. N. Xu, X. Yu, Z. Liu, T. Zhang, H. Chu, *Energy*, **294**, 130818 (2024) https://doi.org/10.1016/j.energy.2024.130818
32. P. Zlateva, A. Terziev, M. Murzova, N. Mileva, M. Vassilev, *Energies*, **18**(15), 4153 (2025) https://doi.org/10.3390/en18154153
33. A. Idir, R. Younes, M. A. Bradai, A. Sadeddine, L. Baiamonte, G. Pintaude, *Coatings*, **13**, 878 (2023) https://doi.org/10.3390/coatings13050878
34. A. Wypych, T. Jankowiak, W. Sumelka, *Materials*, **16**, 7566 (2023) https://doi.org/10.3390/ma16247566
35. R. Bhaskaran Nair, R. Supekar, S. Morteza Javid, W. Wang, Y. Zou, A. McDonald, J. Mostaghimi, P. Stoyanov, *Metals*, **13**, 579 (2023) https://doi.org/10.3390/met13030579
36. M. Bellippady, S. Björklund, X. H. Li, R. Frykholm, B. Kjellman, S. Joshi, N. Markocsan, *Coatings*, **14**, 626 (2024) https://doi.org/10.3390/coatings14050626
37. M. Oksa, E. Turunen, T. Suhonen, T. Varis, S. P. Hannula, *Coatings*, **1**, 17 (2011) https://doi.org/10.3390/coatings1010017
38. A. Garfias Bulnes, V. Albaladejo Fuentes, I. Garcia Cano, S. Dosta, *Coatings*, **10**, 1157 (2020) https://doi.org/10.3390/coatings10121157
39. A. A. Genbach, D. Yu. Bondartsev, H. I. Beloev, *IOP Conf. Ser.*: *Mater. Sci. Eng.*, **1032**, 012039 (2021) doi:10.1088/1757-899X/1032/1/012039
40. A. Javan, W. R. Bennet, D. Herriot, *Physical Review Letters*, **6**, 106 (1961) https://doi.org/10.1103/PhysRevLett.6.106